
Article:
Yeandel, S. orcid.org/0000-0002-6977-1677, Freeman, C. and Harding, J. orcid.org/0000-0001-8429-3151 (2022) A general method for calculating solid/liquid interfacial free energies from atomistic simulations: application to CaSO4.xH2O. The Journal of Chemical Physics, 157 (8). 084117. ISSN 0021-9606

https://doi.org/10.1063/5.0095130

The Journal of Chemical Physics

A general method for calculating solid/liquid interfacial free energies from atomistic simulations: Application to $CaSO_4 \cdot xH_2O$

Cite as: J. Chem. Phys. **157**, 084117 (2022); https://doi.org/10.1063/5.0095130
Submitted: 08 April 2022 • Accepted: 02 June 2022 • Accepted Manuscript Online: 02 June 2022 • Published Online: 25 August 2022

Published open access through an agreement with JISC Collections

Stephen R. Yeandel, Colin L. Freeman and John H. Harding

The Journal of Chemical Physics ARTICLE scitation.org/journal/jcp

A general method for calculating solid/liquid interfacial free energies from atomistic simulations: Application to $CaSO_4 \cdot xH_2O$

Cite as: J. Chem. Phys. 157, 084117 (2022); doi: 10.1063/5.0095130
Submitted: 8 April 2022 • Accepted: 2 June 2022 •
Published Online: 25 August 2022

Stephen R. Yeandel,[a] Colin L. Freeman, and John H. Harding

AFFILIATIONS

Department of Materials Science and Engineering, Sir Robert Hadfield Building, University of Sheffield, Mappin Street, Sheffield S1 3JD, United Kingdom

[a]Author to whom correspondence should be addressed: S.Yeandel@Sheffield.ac.uk

ABSTRACT

We present a general method for computing interfacial free energies from atomistic simulations, which is particularly suitable for solid/liquid interfaces. Our method uses an Einstein crystal as a universal reference state and is more flexible than previous approaches. Surfaces with dipoles, complex reconstructions, and miscible species are all easily accommodated within the framework. It may also be extended to calculating the relative free energies of different phases and other types of defect. We have applied our method to interfaces of bassanite and gypsum with water and obtained interfacial free energies of the order of 0.12 J/m^2, of which ~45% is due to entropic contributions. Our calculations of the interfacial free energy of NaCl with water obtained a value of 0.13 J/m^2, of which only 19% is from entropic contributions. We have also predicted equilibrium morphologies for bassanite and gypsum that compare well with experiments and previous calculations.

I. INTRODUCTION

The calculation of interfacial enthalpies is frequently performed in atomistic simulations and used to predict properties such as hydration energies and morphologies. For many materials, however, the enthalpy alone does not give the full picture of what is happening. Entropic contributions also play a role in determining the properties of many systems, particularly those at solid/liquid interfaces, where the solid may impose ordering in the (usually disordered) liquid.[1] By computing the free energy of the interface, the entropic terms are included in addition to the enthalpy.

The calculation of free energies is significantly more challenging than the calculation of enthalpies. Many methods exist to calculate free energies, but they usually depend on a reference state into which the material under study can be transformed. This is straightforward when the system is composed of a single material or is in a single physical state, and a thermodynamic pathway can be easily defined. However, the calculation of interfacial free energies between a solid material and a liquid phase is particularly challenging as many simple thermodynamic pathways are plagued by divergences and hysteresis.

Nevertheless, several ways to compute interfacial free energies have been proposed. The most well-established methods are the so-called "cleaving wall methods."[2–5] These introduce a potential function that is used to separate the solid and liquid components before deactivating the interactions between them. Finally, the solid and liquid components are treated separately to re-form the bulk solid and bulk liquid, respectively. While practical for simple systems, this approach has a few drawbacks. First, it assumes that the top and bottom surfaces of the solid slab will re-form the bulk when they meet, which may not be the case. Second, the cleaving wall relies on there being a flat, well defined, solid/liquid interface. Third, it is difficult to account for dipolar surfaces when a fully periodic system is employed for the liquid/solid/liquid configurations required.[6,7]

Other methods have also been proposed for calculating interfacial free energies, including direct simulation of contact angles,[8] solid–liquid coexistence calculations using metadynamics,[9,10]

"mold integration" approaches,[11–13] non-equilibrium and non-slab geometry approaches,[14] and many others.[15–21] All of these methods have their own drawbacks. For instance the direct simulation of contact angles requires very large simulation cells, the use of metadynamics needs complex order parameters to differentiate solid and liquid phases, and mold integration methods are only suitable near the solid/liquid coexistence point (with respect to temperature or concentration). It is therefore clear that a more general approach is required.

We present a new method for calculating interfacial free energies based on using Einstein crystals[22] as a common reference. Our method can be applied to significantly more complex materials than previous methods as well as to more complex solid/liquid interfaces. Furthermore, it makes extensive re-use of calculated values to significantly improve the efficiency of calculating the interfacial free energy when making a number of different surface cuts of the same material.

The method presented here is similar to the independently developed approach of Addula and Punnathanam[23] but has several key advantages. First, we have optimized our method so that the free energy of cleaving a liquid phase does not have to be calculated explicitly, recognizing that this process is simply the generation of liquid surface and is therefore equal to the free energy of the liquid/vacuum interface multiplied by the surface area. The free energy of the liquid/vacuum interface may therefore be calculated separately by more efficient methods and re-used for every solid/liquid calculation. Second, by employing an additional vacuum gap on either side of the liquid/solid/liquid configurations, we are able to study dipolar surfaces through the use of a dipole correction.[6,7] Finally, and most importantly, our method can deal with miscible molecules at the interface. These are handled by employing a secondary thermodynamic pathway designed specifically to transfer liquid molecules to an Einstein crystal.

II. METHODOLOGY

Most free energies of interest are not defined with respect to an ideal gas (whose absolute free energy is known) but with respect to some other state. Chief among these are defect energies that can include 0D point defects, 1D line defects, 2D grain boundaries or interfaces, and larger 3D defective structures, such as nano-inclusions. The free energy of creating these defects is usually defined with respect to pure bulk phases. There is no reason, however, why another reference cannot be used if it is more convenient. We have chosen Einstein crystals[22] as a common reference state as it is relatively easy to transform solid materials to and from them and calculate the change in free energy.

A. Einstein crystals

In an Einstein crystal, each atom is confined in an independent harmonic potential with a fixed spring constant, and the atoms do not interact with each other.[22] While the Einstein crystal was originally developed to explain experimental observations of heat capacity, the simple nature of the model has lent itself to calculation of free energies.[24,25] The total energy of an Einstein crystal is given by

$$E_{Ein.} = U + K = \sum_i \left(\frac{1}{2}k(\mathbf{r}_i - \mathbf{r}_{i0})^2\right) + \sum_i \left(\frac{1}{2}m_i \mathbf{v}_i \cdot \mathbf{v}_i\right), \quad (1)$$

where U is the configurational energy, K is the kinetic energy, and k is the spring constant. $\mathbf{r}_i$, $\mathbf{r}_{i0}$, $\mathbf{v}_i$, and m_i are the position, minimum energy position, velocity, and mass of atom i, respectively. The total energy of an Einstein crystal does *not* depend on the relative arrangement of the constituent atoms in Cartesian space. The configurational energy, U, depends only on the atom positions within their respective independent harmonic wells and the stiffness of the spring, k. In simple terms, the atoms do not "feel" each other. The kinetic energy, K, is a function of the temperature and also does not depend on relative Cartesian positions of the constituent atoms. This means that an Einstein crystal may be re-arranged at will with no change to the total energy. For fixed composition, temperature, and k, the total energy of any possible arrangement of the species in an Einstein crystal in Cartesian space is the same. This permits a unified approach to calculating the free energy difference between two systems "A" and "B" of the same composition.

In general, the free energy of transforming system "A" into system "B" (ΔF_A^B), may be computed by transforming between the systems along a continuous and reversible thermodynamic pathway using thermodynamic integration (see Appendix A). Rather than attempting to directly transform system "A" into system "B" using some hard to define thermodynamic pathway, we can instead transform in two stages using an Einstein crystal intermediate,

$$\Delta F_A^B = \Delta F_A^{Ein.(A)} + \Delta F_{Ein.(A)}^B, \quad (2)$$

where $\Delta F_A^{Ein.(A)}$ is the free energy difference between system "A" and the Einstein crystal with the same atomic configuration, "$Ein.(A)$." Similarly, $\Delta F_{Ein.(A)}^B$ is the free energy difference between the Einstein crystal "$Ein.(A)$" and system "B." Since the free energy is a function of state, we can obviously write

$$\Delta F_A^B = \Delta F_A^{Ein.(A)} + \Delta F_{Ein.(A)}^{Ein.(B)} + \Delta F_{Ein.(B)}^B, \quad (3)$$

where "$Ein.(B)$" is the Einstein crystal with the same atomic configuration of system "B." Since we know that $\Delta F_{Ein.(A)}^{Ein.(B)} = 0$ from the argument above and since manifestly $\Delta F_B^{Ein.(B)} = -\Delta F_{Ein.(B)}^B$, we obtain the following equivalent expression [noting that we can drop the distinction between $Ein.(A)$ and $Ein.(B)$]:

$$\Delta F_A^B = \Delta F_A^{Ein.} - \Delta F_B^{Ein.}, \quad (4)$$

where we now have the transformation of system "B" to an Einstein crystal as well. Equation (4) is entirely equivalent to Eq. (2), except that it makes clear that the re-arrangement of the Einstein crystal makes no contribution to the free energy, greatly simplifying the calculation. A further advantage of this approach is that if a large number of relative free energies are required (i.e., multiple "B" states), multiple transformations of "A" are not required since all configurations are transformed by way of the Einstein crystal. Another useful property is that the systems "A" and "B" need not have identical numbers of atoms due to the extensive property of free energies. This means that as long as systems "A" and "B"

have the same stoichiometric ratio of atoms, the free energies can be scaled. This can be particularly advantageous for systems with multiple phases where the unit cells contain different numbers of atoms.

The use of Einstein crystals as a universal reference may be extended to multi-component systems. For two systems "A" and "B" that may be combined to form system "C",

$$\Delta F^{C}_{A+B} = \Delta F^{Ein.(A)}_{A} + \Delta F^{Ein.(B)}_{B} - \Delta F^{Ein.(C)}_{C}, \tag{5}$$

where we now differentiate between Einstein crystals of different stoichiometry. Once again, this a highly efficient way to compute the relative free energy if there are multiple "C" states that need to be computed.

Although we are combining two Einstein crystals, an additional "entropy of mixing" term is not required. As each atom is transferred to an Einstein crystal, the region of space it is able to explore is reduced to a small volume, effectively "de-mixing" the system. The "entropy of mixing" is thus included in the transfer to an Einstein crystal, and the free energy change upon combining Einstein crystals is zero,

$$\Delta F^{Ein.(C)}_{Ein.(A)+Ein.(B)} = 0. \tag{6}$$

For notational convenience, we will no longer distinguish between Einstein crystals of different stoichiometries. Instead, the Einstein crystal will be assumed to be the same stoichiometry as the system identified in the subscript,

$$\Delta F^{Ein.(C)}_{C} = \Delta F^{Ein.}_{C}. \tag{7}$$

The power of using an Einstein crystal as an intermediate state comes from never having to re-arrange atoms. Only the start and end states are needed, and complex thermodynamic pathways between them need not be devised. This greatly simplifies the calculation of relative free energies of systems, which include defects, defect clusters, surfaces, and interfaces. These may contain very complex structural reconstructions, and a simple thermodynamic pathway may not be obvious. The only requirement is that the systems of interest must be convertible to an Einstein crystal. This is trivial for solid systems (Sec. II D), but extra care must be taken for liquids (Sec. II F). To compute the relative free energy of transforming a system into an Einstein crystal, we use the Thermodynamic Integration (TI) method as explained in Appendix A.

Finally, we note that as we are calculating free energy *differences* between systems of the same stoichiometry, any combinatorial terms arising from exchange of particles cancel out. This extends to the three-component system described by Eq. (5) where systems "A" and "B" may be considered a single system "$A + B$" with two non-interacting halves and the same stoichiometry as system "C."

B. Interfacial free energies

We start with a solid slab in the middle of the simulation cell sandwiched between two liquid layers on either side. The rest of the simulation cell contains a significant volume of vacuum, and the liquid/slab/liquid configuration does not extend across a periodic boundary, allowing the use of a dipole correction if required.[6,7] This system is equilibrated with the lattice vector perpendicular to the slab fixed. The average lattice vectors parallel to the surface are calculated and then fixed for all subsequent simulations. Although two liquid/vacuum interfaces are present in the system, these do not change along the thermodynamic pathway and so their contribution to the free energy change will be zero.

The method we have developed is best understood as starting from bulk solid and a single thick liquid layer and constructing the liquid/slab/liquid system shown in Fig. 1. We start with the single thick liquid layer and generate a vacuum gap in the middle, large enough to accommodate the solid slab ($\Delta F^{Liquid+Vacuum}_{Liquid}$). Next, we transfer the bulk solid into the vacuum gap, expressing the desired surface in contact with the two liquid layers (ΔF^{Slab}_{Bulk}). Dividing by twice the surface area, A, of the simulation cell (because we have generated two interfaces), we obtain

$$\gamma_{Interface} = \frac{\Delta F^{Liquid+Vacuum}_{Liquid} + \Delta F^{Slab}_{Bulk}}{2A}, \tag{8}$$

where $\gamma_{Interface}$ is the interfacial free energy of the solid/liquid interface. To facilitate the transformation of the bulk solid into a slab inside the vacuum gap, we use an Einstein crystal (Sec. II A) and write the free energy as

$$\Delta F^{Slab}_{Bulk} = \Delta F^{Ein.}_{Bulk} - \Delta F^{Ein.}_{Slab}. \tag{9}$$

Equation (9) allows the use of the existing bulk solid and liquid/slab/liquid systems. The bulk solid and the solid component of the liquid/slab/liquid system are both transformed to an Einstein crystal, as outlined in Secs. II D and II E, to obtain $\Delta F^{Ein.}_{Bulk}$ and $\Delta F^{Ein.}_{Slab}$, respectively. The free energy of transforming the bulk solid to an Einstein crystal, $\Delta F^{Ein.}_{Bulk}$, may be calculated once and scaled for different slab geometries as required.

Since all Einstein crystals of a given composition have the same free energy (Sec. II A), an explicit rearrangement of the atoms from bulk solid to the solid slab is not required. Moreover, it is no longer a requirement that the top and bottom surfaces of the solid slab meet to re-form the bulk solid. Complex surface reconstructions are handled as easily as more simple surfaces as they do not need to be coaxed into being more bulk-like.

Using Eq. (9) in Eq. (8) and rearranging give

$$\gamma_{Interface} = \frac{\Delta F^{Liquid+Vacuum}_{Liquid}}{2A} + \frac{\Delta F^{Ein.}_{Bulk} - \Delta F^{Ein.}_{Slab}}{2A}. \tag{10}$$

The first term on the right-hand side of Eq. (10) corresponds to the splitting of a single liquid slab into two liquid slabs with a vacuum gap between them, divided by the total surface area of the newly created liquid/vacuum interfaces. This is simply the surface free energy of the liquid in contact with a vacuum, γ_{Liquid}, which for liquids is equivalent to the surface tension (Appendix B). Simplifying Eq. (10), we have

$$\gamma_{Interface} = \gamma_{Liquid} + \frac{\Delta F^{Ein.}_{Bulk} - \Delta F^{Ein.}_{Slab}}{2A}. \tag{11}$$

The liquid surface free energy, γ_{Liquid}, can also be computed once and re-used for multiple surface configurations.

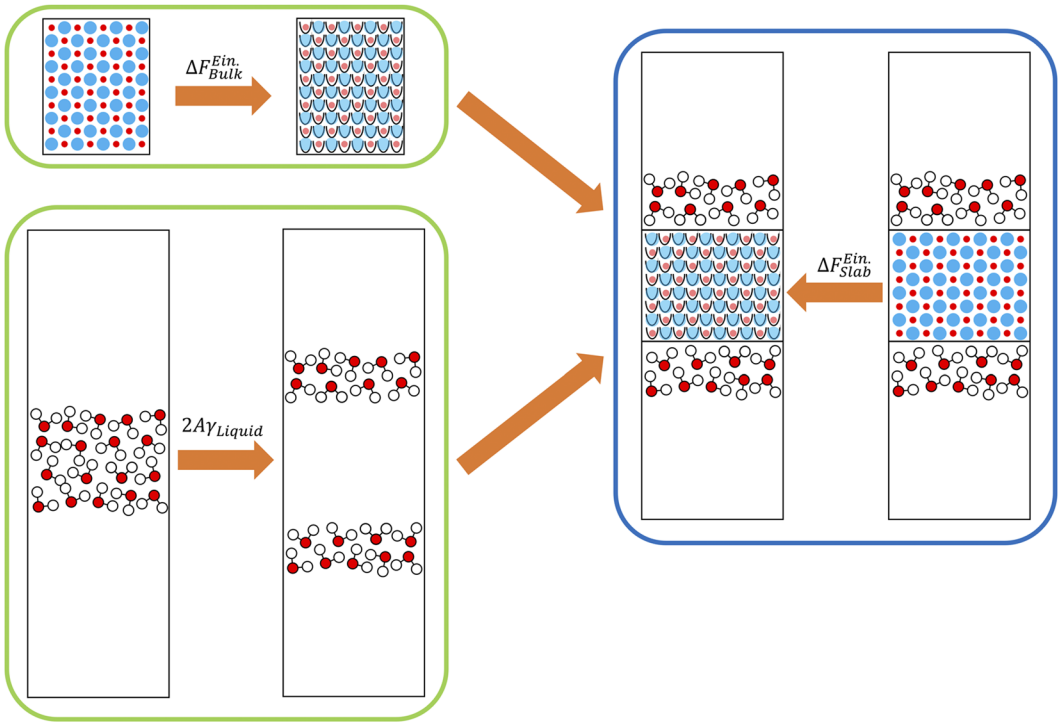

FIG. 1. Flow diagram for computing interfacial free energies. Terms in green boxes may be computed once and re-used. Terms in the blue box are computed for each slab configuration. Note that all terms will be divided by 2*A* to obtain the interfacial free energy, obtaining Eq. (11). The additional $N\Delta f_{Liquid}^{Ein.}$ term included in Eq. (12) has been omitted for clarity.

Equation (11) is applicable to most well-defined solid/liquid interfaces. In certain cases, however, the solid may contain species (ions/molecules) that, although they formally belong to the solid slab to maintain constant composition, behave as a liquid at the interface, for example, crystals containing water of crystallization. In these cases, the miscible species should not be transferred directly to an Einstein crystal along with the solid slab, as this will create a divergence in the thermodynamic integration (Sec. II F). Instead, the miscible species should be treated as part of the liquid layer, and a correction is applied to account for the free energy of taking the miscible species from the liquid layer and transferring it to an Einstein crystal, restoring the stoichiometry. This is a complex process, and a detailed discussion of how this is achieved is given in Sec. II F.

The final equation with this correction is given by

$$\gamma_{Interface} = \gamma_{Liquid} + \frac{\Delta F_{Bulk}^{Ein.} - \Delta F_{Slab}^{Ein.} - N\Delta f_{Liquid}^{Ein.}}{2A}, \tag{12}$$

where N is the number of miscible species that need to be transferred from the liquid to restore stoichiometry of the Einstein crystal and $\Delta f_{Liquid}^{Ein.}$ is the free energy per-species of taking the miscible species from the liquid state to an Einstein crystal.

Equation (12) has been developed to allow for extensive re-use of computed free energy values, which enables an efficient workflow for calculating interfacial free energies of different surfaces. The workflow of our method is presented in Fig. 1 and may be summarized as follows:

1. Compute γ_{Liquid} using the method outlined in Sec. II C.
2. Compute $\Delta F_{Bulk}^{Ein.}$ using the method outlined in Sec. II D.
3. Compute $\Delta F_{Slab}^{Ein.}$ (and the surface area A) for each desired surface configuration via the method outlined in Sec. II E.
4. Compute the correction $\Delta f_{Liquid}^{Ein.}$ using the method outlined in Sec. II F if required (not shown in Fig. 1).

The values of γ_{Liquid}, $\Delta F_{Bulk}^{Ein.}$, and $\Delta f_{Liquid}^{Ein.}$ are computed once and re-used for multiple different slab calculations that utilize the same bulk solid and liquid but differ only in the expressed surface of the slab. $\Delta F_{Bulk}^{Ein.}$ is scaled to match the composition of each slab considered.

C. Calculation of surface tension of liquids

To calculate the surface free energy (surface tension) of a liquid, we have adopted the approach of Kirkwood and Buff (KB),[26] which only requires information from a single simulation, rather than the multiple simulations needed to form a thermodynamic pathway. First, a system of fixed size and shape is set up, containing a single thick layer of liquid aligned in the *xy* plane with vacuum both above and below, exposing two liquid/vacuum interfaces. The KB

method then relates the components of the pressure tensor to the surface tension by the expression

$$\gamma_{Liquid} = \frac{1}{2}\int_0^{L_z} [P_{zz} - 0.5(P_{xx} + P_{yy})]\, dz, \tag{13}$$

where γ_{Liquid} is the surface tension of the liquid, L_z is the length of the simulation cell in the z direction, and P_{xx}, P_{yy}, and P_{zz} are the diagonal components of the pressure tensor. The integral is performed numerically by dividing the simulation cell into thin slices over the perpendicular direction z and computing the average pressure tensor in each slice. The prefactor of $1/2$ accounts for the presence of two liquid/vacuum interfaces.

Note the KB method is applicable only to fluid interfaces and cannot be used for solids (see Appendix B).

D. Bulk solids to Einstein crystals

The conversion of a bulk solid to an Einstein crystal is generally straightforward as both are in the same physical state. First, a simulation cell containing the bulk solid is prepared and equilibrated under the target conditions, such that the average lattice vectors are correct, using an NPT ensemble. All further calculations are performed under an NVT ensemble and are equilibrated with the total momentum of the system set to zero. Next, a random configuration of the bulk solid is chosen from the molecular dynamics simulation, and the atomic positions are used as the minimum positions of the individual harmonic wells of the Einstein crystal. The minimum positions of the harmonic wells need not be at the lattice sites as long as they are representative of a state accessible to the simulation. From here, the transformation to an Einstein crystal proceeds in two stages:

1. Activate harmonic wells for each atom using TI ($\lambda_{Harm.}$).
2. Deactivate all inter- and intra-molecular interactions simultaneously using TI ($\lambda_{Pot.}$).

In the first stage, the activation is performed by defining a TI pathway between $\lambda_{Harm.} = 0$ and 1 where the harmonic wells are either fully off or on respectively. The TI pathway is broken up into discrete simulations, each with a set $\lambda_{Harm.}$ value. For each simulation, a value of $\partial H(\lambda)/\partial\lambda$ may be obtained and an integral over the TI pathway performed, as outlined in Appendix A, to obtain the free energy change.

In the second stage, the deactivation is performed by defining a TI pathway between $\lambda_{Pot.} = 1$ and 0 where the interactions are either fully on or off respectively (excluding the harmonic wells). As before, the TI pathway is broken up into discrete simulations and evaluated to obtain the free energy change. We have defined $\lambda_{Pot.}$ to control the strength of the interactions, so we take the negative of the integral between $\lambda_{Pot.} = 0$ and 1.

When using TI to transform a solid into an Einstein crystal, there are several considerations to bear in mind. Most important is that the positions of the harmonic wells remain the same at every point along the TI. If the wells are allowed to move between different TI points, then the free energy to contain the atoms in the wells will not be consistent. It is only when all inter-atomic interactions are deactivated that the Cartesian positions of the well have no bearing on the energy. Thus, one should initiate all TI points in both stages with the same atomic configuration and set the positions of the wells to the initial positions of the atoms. An additional benefit of this approach is that all TI points may be computed in parallel.

Although the minima of the harmonic wells are not located at the minimum energy lattice sites of the crystal, the transformation to an Einstein crystal is still consistent. This is because any additional energy required to move the atoms from their minimum energy lattice sites to the harmonic wells of the Einstein crystal in the first stage is later recovered as the interactions are deactivated in the second stage. This is possible because the free energy of all Einstein crystals of a given composition is the same.

Another consideration is that the simultaneous deactivation of all interactions could lead to an inter-atomic interaction stronger than the harmonic wells, resulting in an infinite attraction between two atoms and a divergence in the integral. In practice, the probability of this occurring can be made arbitrarily small by increasing the strength of the harmonic wells (see p. 245 of Frenkel and Smit[25]). In essence, the atoms are protected from collision by being constrained within the harmonic wells.

It is also prudent to maintain charge neutrality throughout the deactivation of the inter-atomic interactions. Altering the net charge across a thermodynamic pathway may require several corrections.[27–30] Additionally, highly charged systems may lead to unstable dynamics and cause the simulation to crash.

Finally, a drift in the center of mass of the solid is possible in the limit of the harmonic wells being completely deactivated[25] ($\lambda_{Harm.} \to 0$), resulting in a divergence in the thermodynamic integration. We avoid this issue in two ways. First, each TI simulation along the pathway (discrete value of λ) is equilibrated to remove any total momentum; thus, drifts in the center of mass can only occur through numerical drift, which is kept small through the use of an appropriate timestep, thermostat, and robust time integration algorithm. Second, we do not use $\lambda_{Harm.}$ directly but instead implement a sigmoid function of $\lambda_{Harm.}$. As discussed in Appendix A, the use of the sigmoid function is equivalent to increased sampling of the TI pathway as $\lambda_{Harm.}$ approaches 0 or 1, ensuring convergence of the thermodynamic integration in the limit $\lambda_{Harm.} \to 0$. Indeed, we see no drift in the center of mass in any of our simulations, and no divergence is observed in the integrand.

In principle, a correction to account for the fixed center of mass of the system is applicable.[25] The origin of these corrections is easily demonstrated when one considers an Einstein crystal comprising one atom with a fixed center of mass. Such a system cannot evolve with time and so the harmonic well of the Einstein crystal is never sampled. However, the size of the correction falls rapidly with increasing numbers of atoms and is negligible for the system sizes we use and the properties we are interested in.

Together, stages 1 and 2 give the value of $\Delta F^{Ein.}_{Bulk}$ in Eq. (12). Because free energy is an extensive property, the transformation of a bulk solid to an Einstein crystal needs to be performed only once for each material. The free energy of the transformation can then be scaled to the size of cell required. This means that this process may also be applied to compute the free energy differences of systems with the same composition as the bulk solid, e.g., the formation of Schottky and Frenkel defects, stacking faults, grain boundaries, and different polymorphs.

E. Solid slabs to Einstein crystals

The transformation of a solid slab to an Einstein crystal is performed in a similar way to that described for bulk solids in Sec. II D with the key difference that we transform the solid component to an Einstein crystal while leaving the liquid layers untouched. We again do this in two stages:

1. Activate harmonic wells on all atoms in the solid state using TI ($\lambda_{Harm.}$).
2. Deactivate solid–solid and solid–liquid interactions simultaneously using TI ($\lambda_{Pot.}$), leaving liquid–liquid interactions in place.

In the first stage, harmonic wells are activated on atoms in the solid state in the same way as discussed in Sec. II D. In the second stage, the solid–solid and solid–liquid interactions are deactivated as described in Sec. II D. The liquid–liquid interactions are fully retained at every stage. Together, stages 1 and 2 give the value of $\Delta F^{Ein.}_{Slab}$ in Eq. (12).

In principle, other procedures are possible, which also transform the solid slab to an Einstein crystal. For example, the solid–liquid interactions could be deactivated first, which would give the free energy of immersion of the dry solid surface. However, the surface configuration of the solid slab in liquid may be significantly different to the configuration in vacuum. If this is the case, there may be a large reconstruction of the surface upon immersion. Such a reconstruction may require long simulation times to converge at each point along the TI pathway. Alternatively, there may be a discontinuity along the pathway and the free energy integral would become ill-defined.

If the free energy of immersion in liquid is needed, then it is once again simpler and more efficient to perform the calculation using an Einstein crystal. The transformation of the immersed slab to an Einstein crystal may be calculated as above, and an additional transformation of a dry solid slab to an Einstein crystal is also calculated. It is then simple to subtract the two computed values and divide by the surface area to obtain the free energy of immersion. This procedure avoids any explicit reconstruction of the slab surface upon immersion and is thus more stable.

One possible problem when transforming an immersed slab into an Einstein crystal is that there is nothing to prevent liquid molecules detaching from the liquid layer and translating through the partially transformed slab. This translation can result in a liquid molecule approaching too closely to a transforming solid atom and experiencing extremely large forces, leading to instabilities in the dynamics and the simulation to crash. This scenario may be prevented by introducing two additional TI stages that add and remove walls to protect the slab during transformation, as was done by Qi, Zhou, and Fichthorn.[5] The modified procedure would then have four stages:

1. Activate harmonic wells on the atoms in the solid state using TI ($\lambda_{Harm.}$).
2. Activate protecting walls at the solid/liquid interface using TI ($\lambda_{Wall\text{-}on}$).
3. Deactivate solid–solid and solid–liquid interactions simultaneously using TI ($\lambda_{Pot.}$), leaving liquid–liquid interactions in place.
4. Deactivate protecting walls at the solid/liquid interface using TI ($\lambda_{Wall\text{-}off}$).

This four-stage procedure is more robust than the two-stage procedure described above but doubles the number of TI pathways that must be computed. For the systems we have tested, the detachment and translation of a liquid molecule through the transforming slab is rare. In such cases, we have simply restarted the simulation with a new random velocity seed, which results in dynamics where the liquid molecule does not detach from the liquid layer.

F. Correction for miscible species

Some solid materials contain miscible species that are very loosely bound at an interface with a liquid and may become part of the liquid layer. These species may be incorporated solvent molecules or ions in equilibrium with the solution. These species must still formally "belong" to the solid slab to maintain constant composition, but they are free to diffuse in the liquid with no fixed equilibrium position. To move these species directly to an Einstein crystal would require integrating across a first-order phase transition. This leads to hysteresis in the thermodynamic pathway, and the free energy integral over the pathway becomes ill-defined. In this section, we will refer to molecules as the general case, but the discussion equally applies to monatomic species.

To avoid the first-order phase transition between the liquid and solid state, we instead transform into another state where the absolute free energy is known analytically, the ideal gas. The absolute free energy of an Einstein crystal is also known analytically and so the connection between the liquid phase and the solid phase can be made while avoiding the divergence. The absolute free energy of an ideal gas of molecules[31] is given by

$$F_{Ideal} = -k_B T \ln\left[\frac{V^N}{N!}\left(\frac{1}{\Lambda^2}\right)^{3N/2}\right], \tag{14}$$

where k_B is Boltzmann's constant, T is the temperature, V is the volume of the system, and N is the number of ideal gas molecules in the system. The thermal de Broglie wavelength is given by

$$\Lambda = \left(\frac{\beta h^2}{2\pi m}\right)^{1/2}, \tag{15}$$

where $\beta = (k_B T)^{-1}$, h is Planck's constant, and m is the mass of the ideal gas molecule. The absolute free energy of an Einstein crystal[32] is given by

$$F_{Ein.} = k_B T \ln\left(\frac{\beta k \Lambda^2}{2\pi}\right)^{3N/2}. \tag{16}$$

Using Eqs. (14) and (16), the free energy of an Einstein crystal with respect to an ideal gas is given by

$$\begin{aligned}\Delta F^{Ein.}_{Ideal} &= F_{Ein.} - F_{Ideal} \\ &= k_B T \ln\left(\frac{\beta k}{2\pi}\right)^{3N/2} + k_B T \ln\left(\frac{V^N}{N!}\right),\end{aligned} \tag{17}$$

where the momentum terms of the free energies have canceled. We may simplify Eq. (17) further as follows:

$$\Delta F_{Ideal}^{Ein.} \approx Nk_BT\left[\frac{3}{2}\ln\left(\frac{\beta k}{2\pi}\right)+\ln\left(\frac{Ve}{N}\right)\right], \tag{18}$$

where we have used Stirling's approximation in the form

$$\begin{aligned}\ln\left(\frac{1}{N!}\right) &\approx N\ln\left(\frac{1}{N}\right)+N\\ &\approx N\ln\left(\frac{e}{N}\right).\end{aligned} \tag{19}$$

The factor of e (Euler's number), which arises in Eq. (18), results in an additional Nk_BT of free energy when transforming an ideal gas to an Einstein crystal. This additional energy is unrelated to either the spring constant of the Einstein crystal, k, or the density of the ideal gas, V/N (which together form a dimensionless argument to the combined logarithm). Its origins lie in the indistinguishability of the molecules in the ideal gas.

In an ideal gas, any two molecules may be exchanged without altering the total energy of the system; they are *indistinguishable*. Conversely, the molecules in an Einstein crystal are tethered to specific points in space by harmonic springs, and the exchange of any two molecules results in the harmonic springs being "stretched." The "stretched" springs increase the total energy of the system, and the molecules are therefore *distinguishable*. The additional Nk_BT of energy arising in Eq. (18) can therefore be thought of as due to the loss of "communal entropy" upon transformation from an ideal gas to an Einstein crystal.[31,33]

To calculate the correction for miscible species, the slab systems generated in Sec. II E should not be used. This is because the liquid layers in the slab system have only a finite thickness, approximating an infinitely thick liquid layer. This approximation is sufficient to capture the effects of liquid ordering at the interface but may not be able to fully account for the entropy available to miscible species. Additionally, for a finitely thick liquid layer, the V/N term in Eq. (18) becomes poorly defined. Using a 3D periodic simulation cell of the bulk liquid approximates the environment deep inside an infinitely thick liquid layer and circumvents both of these issues.

The free energy of transforming a molecule in the liquid state to an Einstein crystal is performed in an NVT ensemble over four stages:

1. Deactivate all inter-molecular interactions using TI ($\lambda_{Inter\text{-}off}$) to form an ideal gas of N molecules.
2. Calculate analytically the free energy to transform an ideal gas of N molecules into an Einstein crystal using Eq. (18).
3. Activate harmonic wells on all non-tethered atoms using TI ($\lambda_{Harm.}$).
4. Deactivate intra-molecular interactions using TI ($\lambda_{Intra\text{-}off}$).

In the first stage of the procedure, all inter-molecular interactions are switched off using TI. This stage transforms the liquid into a non-interacting ideal gas of molecules. At this stage, intra-molecular interactions are retained for two reasons. First, many molecular dynamics codes will return an error for the excessive intra-molecular bond lengths, which will occur as the molecule is broken apart into constituent atoms. Second, the translational degrees of freedom of the non-interacting molecule are completely separable from the internal degrees of freedom;[31] thus, we can treat the whole molecule as an ideal gas particle, ignoring internal vibrations and rotations for the time being.

When deactivating the inter-molecular interactions, care should be taken to avoid potentials with singularities at $r = 0$, e.g., the Lennard-Jones potential.[34,35] In our calculations, we use soft-core potentials,[36] which remove the singularity at $r = 0$. These soft-core potentials deactivate the potential in a non-linear way such that occasional high-force collisions have been traded for frequent low-force collisions, and potential energy sampling does not become harder as the atoms "shrink."

In the second stage, the free energy of transforming an ideal gas of molecules into an Einstein crystal is calculated analytically. The value of N used in Eq. (18) should be the number of ideal gas molecules, *not* the total number of atoms. After this stage, the molecules are conceptually tethered to a specific position in space by a harmonic well. However, the choice of position is arbitrary and has no bearing on the free energy. Likewise, which part of the molecule is tethered to the point in space is also arbitrary. We have made the choice of taking a configuration from the ideal gas calculation and tethering a single atom from each molecule to their initial positions in space.

In the third stage, harmonic wells are activated for all remaining non-tethered atoms in the molecule using TI. Because the remaining atoms are bonded to the tethered atom, they are also localized in space and so the TI process will converge. This stage accounts for the previously ignored internal vibrational and rotational degrees of freedom in the molecule.

In the final stage, the remaining intra-molecular interactions are deactivated by TI. By postponing the deactivation of intra-molecular interactions until harmonic wells have been introduced on all atoms, the computed bond lengths will always be "reasonable", thus avoiding algorithmic errors in the molecular dynamics code.

This procedure is applicable to systems where the liquid layers comprise a single molecular species. For situations where the liquid is a solution of many different species, the procedure must be modified (Appendix C).

Summing the contributions from all four stages gives the free energy change of transforming a liquid into an Einstein crystal, $\Delta F_{Liquid}^{Ein.}$. Dividing this quantity by N gives the free energy of the transformation per molecule, which can be used in Eq. (12),

$$\Delta f_{Liquid}^{Ein.} = \frac{\Delta F_{Liquid}^{Ein.}}{N}. \tag{20}$$

G. Interfacial enthalpies

To calculate the enthalpy of an interface, we begin with the system constructed for the interfacial free energies. For this system, we calculate the average potential energy of the slab system (ΔH_{Slab}) and subtract off the average potential energy of the constituent components, leaving just the enthalpy of the interface. The components to subtract off are the bulk solid enthalpy (ΔH_{Bulk}), bulk liquid enthalpy (ΔH_{Liquid}), and liquid/vacuum interfacial enthalpy ($\Delta H_{Liquid/Vacuum}$). These values are much more straightforward to calculate as just the average potential energy and converge much

quicker than free energy calculations. The interfacial enthalpy is then given by

$$\Delta H_{Interface} = \frac{\Delta H_{Slab} - \Delta H_{Bulk} - \Delta H_{Liquid} - \Delta H_{Liquid/Vacuum}}{2A}, \quad (21)$$

where A is the area of the interface and the multiplication by 2 is to account for the presence of two interfaces. The enthalpy values for the bulk solid and liquid have been scaled to match the amount of each present in the slab system, and the liquid/vacuum interfacial enthalpy has likewise been scaled to the correct surface area (accounting for the presence of two liquid/vacuum interfaces). Here, the reference system can be considered to be the infinitely separated, and therefore non-interacting, atoms. To get to this reference state, we do not go via a continuous thermodynamic pathway but instead simply place the atoms in the desired configuration. While this captures the enthalpic difference between the systems, the entropic difference is entirely neglected.

III. CALCIUM SULFATE HYDRATES

The calcium sulfate hydrate system is an excellent model to demonstrate the advantages of an approach based on using Einstein crystals as a common reference state. Calcium sulfate hydrate exists in three known phases of varying hydration. They are anhydrous anhydrite ($CaSO_4 \cdot 0H_2O$), hemihydrate bassanite ($CaSO_4 \cdot \frac{1}{2}H_2O$), and dihydrate gypsum ($CaSO_4 \cdot 2H_2O$). The presence of strongly binding 2+ ions means that there is likely to be strong ordering of the water layer on the surfaces of the materials. Furthermore, the presence of stoichiometric water in the structure means that there will be water molecules on the surface, which formally belong to the solid but behave as a liquid. The correction required for these miscible species is discussed in Sec. II F.

Bassanite crystallizes in the $I121$ space group,[37] and the structure comprises columns of $CaSO_4$ with channels of water between them. When this water is evacuated, bassanite becomes soluble anhydrite. The space group of bassanite contains no center of inversion, and therefore, surfaces with mirror indices are not necessarily identical (e.g., {1 1 0} and {−1 −1 0}), even if they are structurally very similar. These distinct surfaces may give rise to dipoles in simulations, which must be handled carefully (Sec. III A).

Gypsum, also called calcium sulfate dihydrate, is the most thermodynamically stable calcium sulfate hydrate under ambient conditions.[38] It crystallizes in the $C12/c1$ space group.[39] This space group contains a center of inversion, and therefore, surfaces with mirror indices are always identical. In experiments, it is often observed that bassanite forms first, followed by gypsum.[38,40]

Anhydrite is the anhydrous phase, which is most thermodynamically stable at high temperatures.[38] At ambient conditions, there are two possible forms. Insoluble anhydrite[41] (space group *Amma*) is formed naturally on the Earth's surface, whereas soluble anhydrite[42] (space group $P6_222$) is formed by dehydrating bassanite.

There is a large degree of uncertainty over the solubility of anhydrite in experiments due to very slow kinetics below 80 °C.[43] In addition, the potential model we employ[44] performs poorly when used to predict the dissolution free energies of the anhydrous phases. We will therefore not consider anhydrite further in this work.

The interfacial free energy is a key property for understanding the nucleation and growth of the calcium sulfate phases in solution. Under classical nucleation theory, the free energy barrier to nucleation is a function of the bulk free energy of the crystal nucleus and the interfacial free energy between the nucleus and the surrounding medium.[45] By computing the relative free energy of different phases and their interfaces with solution, we can predict which phase is more likely to nucleate.

A. Simulation methodology applied to the calcium sulfate hydrates

We constructed the low index surfaces of both bassanite and gypsum and relaxed them with the Minimum Energy Technique Applied to Dislocation, Interface, and Surface Energies (METADISE) code[46] to give an estimate of which surfaces were likely to be the most stable. We also selected a number of experimentally observed surfaces that were slightly higher in energy in our preliminary calculations.

From the selected surfaces, slabs were constructed for use in molecular dynamics simulations. The slab simulation cells were set up such that the x direction was perpendicular to the slab surface. The slabs were ~30 Å thick with 30 Å of water on each surface. The total x direction cell size was 200 Å. For gypsum, the top and bottom surfaces of the slab were identical, but for bassanite, the top and bottom surfaces are different (although frequently similar) for many of the slabs, and so the calculated interfacial free energies are an average of the top and bottom surfaces.

Molecular dynamics simulations were performed using the Large-scale Atomic/Molecular Massively Parallel Simulator (LAMMPS) code.[47] All simulations were performed with a 1 fs timestep at 300 K and 0 bar. Long-ranged electrostatic interactions were computed using the Particle–Particle Particle–Mesh (PPPM) algorithm[48] with a relative force accuracy of 1.0×10^{-5}. For our slab calculations, we also applied the dipole correction of Ballenegger, Arnold, and Cerda.[6,7] This correction is available in LAMMPS natively but only for orthorhombic systems. Hence, we implemented the correction using a script written with LAMMPS commands, which is able to perform the correction for non-orthorhombic systems and which can be applied in any orientation. The script was thoroughly tested against the internal LAMMPS correction and found to give the same results.

Each bulk and slab configuration was equilibrated at constant NPT, using a Nosé–Hoover thermostat and barostat[49,50] (0.1 and 1.0 ps relaxation times respectively), in order to obtain average lattice vectors under the given conditions. Bulk solid cells were equilibrated using full triclinic NPT simulations, with all lengths and angles allowed to vary. Bulk liquid cells were equilibrated using isotropic NPT simulations, where the lengths of the lattice vectors are only allowed to vary in tandem. Slab geometry cells were equilibrated with partial triclinic NPT simulations, where only the y, z, and yx components of the lattice vectors were allowed to vary, keeping the periodic slab distance and alignment fixed. The NPT simulations were equilibrated for 100 ps, followed by 500 ps of production simulation where the lattice vectors were recorded every 100 fs. The average lattice vectors were then calculated and applied for all following calculations.

For the free energy calculations (ΔF), we switched to a Langevin thermostat[51] (0.1 ps relaxation time). Additionally, the random forces applied by the Langevin thermostat are constrained such that the total applied force is zero, ensuring no drift of the

center of mass (see Sec. II D). The switch to a Langevin thermostat is important because near the end of the TI pathway, the system is composed of almost pure harmonic oscillators, for which the Nosé–Hoover thermostat does not provide ergodic sampling.[50,52]

The full thermodynamic pathway of transforming solid bulk/slabs into Einstein crystals was divided into two stages, as outlined in Sec. II D. Each stage was subdivided into 128 equal intervals. The Einstein crystal used a k of 10.0 eV/Å^2 for the harmonic wells, regardless of the atom type.

The correction for miscible water molecules from the bulk solids was performed using the four-stage method outlined in Sec. II F. The thermodynamic pathways of each stage (except the analytical step) used 128 equal intervals per stage. The liquid water simulation cell comprised 3200 water molecules in a cubic box of ~45.7 Å per side. The Einstein crystal once again used a k of 10.0 eV/Å^2 for all atoms to maintain consistency with all other calculations.

Each point along the TI pathways was first equilibrated for 100 ps followed by a 500 ps data collection phase. During the data collection phase, the potential energy was sampled every 1 ps. The derivative $\partial H(\lambda)/\partial\lambda$ was computed by finite differences, as outlined in Appendix A.

The enthalpy calculations (ΔH) were performed using the same setup as for free energy calculations to avoid errors associated with different thermostatting or data sampling. In essence, they are identical to a single point on the thermodynamic pathway where the Einstein crystal is fully off and the potential fully on. While this is technically an average configurational energy, the kinetic energy contributions cancel and the PV term is negligible due to the equilibrated lattice and zero pressure, and so we use it as an enthalpy. The interfacial enthalpy was then computed, as described in Sec. II G. We then simply subtract the interfacial enthalpies from the interfacial free energies to obtain the interfacial entropy component ($-T\Delta S$).

B. Potential model

We use the potential model of Byrne, Raiteri, and Gale[44] (FF1, Force Field 1), which has been fitted to reproduce the solvation free energies of Ca^{2+} and SO_4^{2-} and utilizes the popular SPC/Fw (Simple Point-Charge / Flexible water) model of water.[53] This $CaSO_4 \cdot xH_2O$ potential model has also recently been used to study small clusters of $CaSO_4 \cdot xH_2O$.[54]

Two minor modifications to the potential model were made. First, we opted not to use the long-range van der Waals (vdW) correction available in many molecular dynamics codes.[55,56] This correction is to compensate for the finite cutoff of pair interactions. However, the long-range vdW correction is only applicable for a 3D isotropic and homogeneous system where the radial distribution function (RDF) tends to unity at long distances. In the majority of our systems, we have a 2D slab geometry where these conditions are not met. Therefore, to maintain consistency, we have not applied the long-range vdW correction to any of our simulations. As the potential model of Byrne, Raiteri, and Gale makes heavy use of the Mei-Davenport-Fernando (MDF) taper function,[57] this change only affects the water–water interactions. To compensate, we make a second modification of the potential model where we increase the interaction cutoff distance for water–water interactions to 12 Å, which we found balanced accuracy and speed [similar to the conclusions of an investigation by Pascal and Goddard[58] into the related Simple Point Charge / Extended (SPC/Ew) water model].

We verified our implementation of the potential model by successfully reproducing the lattice parameters as calculated by Byrne, Raiteri, and Gale. We further verified our model by computing the surface tension of water (Sec. IV A) and by comparing the free energy of transforming bulk bassanite into gypsum (Sec. IV B).

IV. RESULTS AND DISCUSSION

A. Surface tension of H_2O

To compute the interfacial free energy of $CaSO_4 \cdot xH_2O$ in water using the method proposed in Sec. II B, we require the surface tension of our water model (SPC/Fw[53]). The surface tension of a liquid/vacuum interface (γ_{Liquid}) may be calculated in a straightforward manner by the Kirkwood–Buff method outlined in Sec. II C.

Ten simulation cells were constructed, which each contained 25 600 water molecules. All cells are orthorhombic with lattice parameters of 80 × 80 × 400 Å^3. This configuration results in a slab of liquid water ~120 Å thick parallel to the xy plane. The simulation cells were divided up into 4000 bins in the z direction of 0.1 Å thickness each. Within each bin, the average local pressure tensor was computed. The simulation cells were each run for 500 ps under NVT conditions with a Langevin thermostat (0.1 ps relaxation time). The dipole correction of Ballenegger, Arnold, and Cerda[6,7] was applied to remove any instantaneous dipole–dipole interactions and maintain consistency with all our other slab geometry simulations. The computed local pressure tensors were used in Eq. (13) to calculate the surface tension of the water slabs.

From this set of calculations, we obtained an average surface tension of 58.1 ± 0.79 mN/m (0.0581 J/m^2) for the SPC/Fw model of water. This compares well to the computed value of 58.6 mN/m (0.0586 J/m^2) in a recent publication by Kadaoluwa Pathirannahalage *et al.*[59] The calculated surface tension of the SPC/Fw water model (58.1 mN/m) is somewhat lower than the experimental value of 71.99 mN/m.[60] However, this is not significantly worse than many other available water models.[59] Indeed, for its simplicity, SPC/Fw does remarkably well for many properties of water.

B. Free energy of transforming bassanite into gypsum

The applicability of an Einstein crystal extends beyond just the calculation of interfacial free energies but can also be used to link bulk phases together. The only chemical difference between the $CaSO_4 \cdot xH_2O$ phases is the proportion of incorporated water. The calculation of the free energy change of transforming a bulk solid to an Einstein crystal is discussed in Sec. II D. Likewise, the method to calculate the free energy change of transforming a liquid to an Einstein crystal is given in Sec. II F. These values have been computed for bassanite, gypsum, and water and are presented in Table I.

Combining the free energy to transfer bulk bassanite and gypsum into Einstein crystals with transferring a liquid water molecule to an Einstein crystal, we may write the expression

$$\Delta F^{Gyp.}_{Bas.} = \Delta F^{Ein.}_{Bas.} + 1.5\Delta F^{Ein.}_{Water} - \Delta F^{Ein.}_{Gyp.}. \quad (22)$$

TABLE I. Free energy change to transform each material to an Einstein crystal (kJ/mol).

Material	$\Delta F_{Bulk}^{Ein.}$
Bassanite ($CaSO_4 \cdot \frac{1}{2}H_2O$)	2665.96
Gypsum ($CaSO_4 \cdot 2H_2O$)	2782.70
Water (H_2O)	76.43

From this expression, we can compute the free energy of transforming one formula unit of bassanite into gypsum to be −2.09 kJ/mol. This transformation may be written concisely as the chemical reaction

$$CaSO_4 \cdot \frac{1}{2}H_2O + 1.5H_2O \xrightarrow[-2.09\text{kJ/mol}]{\Delta F_{Bas.}^{Gyp.}} CaSO_4 \cdot 2H_2O. \quad (23)$$

The free energy of transforming bassanite into gypsum may also be obtained by taking the difference in the dissolution free energies of bassanite and gypsum calculated by Byrne, Raiteri, and Gale.[44] Calculating this difference yields a raw $\Delta F_{Bas.}^{Gyp.}$ of −6.13 kJ/mol at 298.15 K. However, upon dissolution of either phase, the water contained in each material will become indistinguishable from the water already present in the liquid. This leads to a further correction of $1.5k_BT$ due to the addition of 1.5 water molecules into the material upon hydration and the loss of the associated communal entropy as discussed in Sec. II F [Eq. (18)]. Applying this correction to the dissolution free energies of Byrne, Raiteri, and Gale leads to a $\Delta F_{Bas.}^{Gyp.}$ of −2.39 kJ/mol, in excellent agreement with our calculations. These values are also in reasonable agreement with the experimental value of −4.85 kJ/mol computed from the National Bureau of Standards (NBS) tables.[61]

C. Interfacial free energies between $CaSO_4 \cdot xH_2O$ phases and water

The interfacial free energy of bassanite with water was calculated using the methods outlined in Sec. II E. Nine different Miller indices were chosen and calculated as described above (Sec. III A), plus one additional surface reconstruction of the {1 1 0} surface. By comparing the interfacial free energies calculated using 64 and 128 intervals per stage of the thermodynamic integration (Appendix A), we estimate that our bassanite/water interfacial free energies are converged to within ∼0.005 J/m^2, within the expected accuracy of the potential model. The calculated interfacial free energies of the bassanite/water interfaces are given in Table II.

The calculated enthalpic and entropic contributions to the interfacial free energy are both positive. The enthalpic contribution is generally very small due to the strong binding of water by the Ca^{2+} ions, which reduces the energy cost of creating the interface. However, the strong binding of water induces significant ordering in the water layers, resulting in the loss of entropy compared to the bulk liquid ($\Delta S < 0$) and a strong entropic destabilization of the interface. Entropic contributions to the interfacial free energy vary between 41% and 88% of the total interfacial free energy.

TABLE II. Interfacial energies of bassanite/water interfaces (J/m^2). Free energies are calculated with Eq. (12) ($\Delta F = \gamma_{Interface}$), and enthalpies are calculated with Eq. (21) ($\Delta H = \Delta H_{Interface}$). The entropic contribution is obtained by subtraction.

Miller index	Free energy ΔF	Enthalpy ΔH	Entropy $-T\Delta S$
{1 1 0}/{−1 −1 0}	0.0780	0.0283	0.0496
{1 1 0}/{−1 −1 0} (FLAT)	0.1374	0.0810	0.0564
{1 0 0}	0.0741	0.0253	0.0488
{0 −1 0}/{0 1 0}	0.1181	0.0620	0.0561
{0 0 1}	0.1697	0.0645	0.1052
{2 1 0}/{−2 −1 0}	0.1164	0.0584	0.0579
{−3 1 0}/{3 −1 0}	0.1272	0.0667	0.0604
{1 2 0}/{−1 −2 0}	0.1117	0.0566	0.0551
{1 1 −1}/{−1 −1 1}	0.1283	0.0337	0.0946
{2 0 1}	0.1156	0.0138	0.1018

We simulated two forms of the bassanite {1 1 0} surface. The first, displayed in Fig. 2, is very rough, displaying surface crenellations of $CaSO_4$ chains. The second has the crenellations removed, which we term the "FLAT" surface. It is clear from Table II that the crenellated surface is much more stable, primarily due to lowered enthalpic contributions. This can be accounted for by the increased surface area exposed by the $CaSO_4$ crenellations for binding to water. Interestingly, the entropy contributions to the free energies are very similar for the two surfaces, suggesting that the ordering of water is similar for each surface. This can be reconciled with the very different surface structures by considering water ordering beyond the first adsorbed layer. Figure 2 shows the probability density of finding the oxygen atom of a water molecule, as calculated from a molecular dynamics simulation of the crenellated bassanite {1 1 0}/{−1 −1 0}

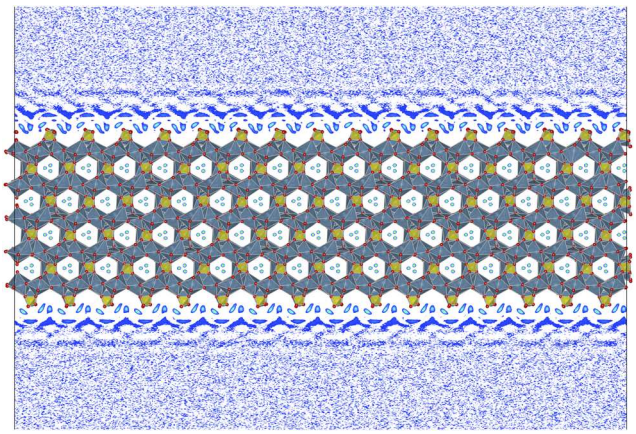

FIG. 2. Probability density of finding O from H_2O on the bassanite {1 1 0}/{−1 −1 0} surfaces. Calcium ions are displayed in dark blue, sulfur in yellow, and oxygen in red. Although the top and bottom surfaces appear almost identical, the lack of inversion symmetry means that they are not. There are almost imperceptible differences in the probability of finding an oxygen atom at different surfaces, arising from the small dipole moment.

TABLE III. Interfacial energies of gypsum/water interfaces (J/m^2). Free energies are calculated with Eq. (12) ($\Delta F = \gamma_{Interface}$), and enthalpies are calculated with Eq. (21) ($\Delta H = \Delta H_{Interface}$). The entropic contribution is obtained by subtraction.

Miller index	Free energy ΔF	Enthalpy ΔH	Entropy $-T\Delta S$
{0 0 1}	0.1421	0.1083	0.0338
{0 1 0}	0.0444	0.0554	−0.0111
{0 1 1}	0.1344	0.1042	0.0302
{0 1 2}	0.1393	0.1080	0.0313
{0 2 1}	0.1198	0.0965	0.0233
{1 1 0}	0.0799	0.0324	0.0475
{−1 −1 1}	0.1762	0.1023	0.0739
{1 2 0}	0.0962	0.0637	0.0325
{−2 2 1}	0.1422	0.0651	0.0772

surface. Figure 2 shows that there is a large degree of water ordering some distance into the water layers, which must contribute to the entropy component of the interfacial free energy.

Nine gypsum/water interfaces were also constructed and simulated in the same way as the bassanite/water interfaces. In the case of gypsum, the symmetry of the crystal means that there is a center of inversion symmetry, and therefore, the top and bottom surfaces are identical. Again, we compare the interfacial free energies calculated using 64 and 128 intervals per stage of the thermodynamic integration (Appendix A) and estimate that the gypsum/water interfacial free energies are converged to within ~0.001 J/m^2, well within the expected accuracy of the potential model. The calculated interfacial free energies of the gypsum/water interfaces are given in Table III.

The interfacial free energies of gypsum surfaces are, in general, very similar to those of bassanite. However, the {0 1 0} surface displays an unusual negative entropy contribution to the interfacial free energy ($-T\Delta S$ i.e., $\Delta S > 0$). We attribute this to the highly structured water layers present in the gypsum structure, which are exposed upon cleaving the [0 1 0] plane. As these water molecules gain disorder upon cleaving their entropy increases, their contribution to the free energy becomes negative. The remaining surfaces of gypsum all have positive entropy contributions to the free energy of between 19% and 59%, significantly lower than for bassanite. Our interfacial entropies range from 0.023 to 0.105 J/m^2 for both materials, up to an order of magnitude higher than Mishra *et al.*[62] who estimated an entropy contribution of 0.015 J/m^2 for calcium sulfates in general. The significant difference arises because Mishra *et al.* assumed that only the first water layer on the surface contributes to the reduction in water entropy. Our simulations show that the ordering of water molecules extends quite far into the liquid (Fig. 2). Furthermore, Mishra *et al.* used the method of Kirkwood and Buff to compute a rough interfacial free energy to support their arguments. However, this method is not applicable to interfaces that contain a solid component (see Appendix B).

D. Interfacial free energy between NaCl and water

To demonstrate the effect of the charge of the cations on the entropy of the solvent, we also simulated NaCl where the bulk solid only has 1+ cations. We used the model of Joung and Cheatham[63] and retained the SPC/Fw water model.[53] We selected the {1 0 0} surface as the most stable surface[64] of NaCl and applied exactly the same procedure as we did for $CaSO_4 \cdot xH_2O$. We calculated the {1 0 0} NaCl/water interface to have an interfacial free energy of 0.128 J/m^2. Our computed interfacial free energy compares well with the results of Espinosa *et al.*[12] of about 0.1 J/m^2, which were obtained with a different potential model and is calculated between bulk NaCl and a saturated solution.

For the NaCl/water system, the contributions of enthalpy and entropy to the interfacial free energy are 0.104 and 0.024 J/m^2, respectively. This is a marked difference to the $CaSO_4 \cdot xH_2O$ systems as here the enthalpic contribution dominates and the entropic contribution is relatively small. The origin of this change is due to the reduced binding of water to the ±1 cation/anion in NaCl. Water is not as strongly bound to the NaCl surface, and there is clearly less ordering when the probability density of finding O from H_2O is calculated (Fig. 3).

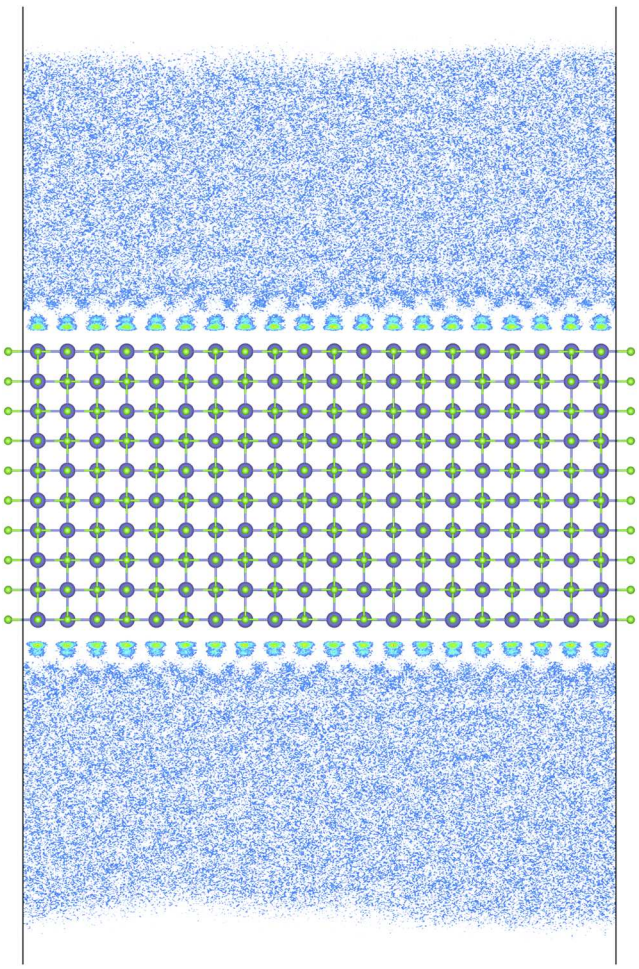

FIG. 3. Probability density of finding O from H_2O on the NaCl {1 0 0} surface. Sodium ions are displayed in purple and chlorine in green. One layer of higher water density is clearly visible, with an additional layer partially visible.

E. Thermodynamic morphologies and growth of $CaSO_4 \cdot xH_2O$ phases

Using the interfacial free energies calculated in Sec. IV C, we may predict the equilibrium morphologies of bassanite and gypsum using a Wulff construction.[65] These equilibrium morphologies are of the material in a solution of pure water. The equilibrium morphologies of bassanite and gypsum are given in Fig. 4.

The bassanite morphology (Fig. 4(a)) is a near-perfect hexagonal prism capped with trigonal pyramids that are truncated by the {0 0 1} Miller plane. The sides of the prism comprise the {1 1 0}/{−1 −1 0} surface pair (Fig. 2) along with the {1 0 0} (non-dipolar) surface, which has a very similar structural motif. This near-perfect hexagonal morphology is not surprising as, although bassanite exhibits an $I121$ monoclinic space group, it is strongly pseudo-trigonal ($P3_121$).[37] The aspect ratio of the bassanite morphology predicted here is smaller than that most commonly seen experimentally. A higher aspect ratio may be achieved by simple stabilization of the near identical {1 1 0}, {−1 −1 0}, and {1 0 0} surfaces, perhaps with surface modification or reconstruction.

This bassanite morphology is similar to that seen by Kong *et al.*[66] when bassanite is grown in reverse microemulsions. In the conditions used by Kong *et al.*, the grown bassanite crystals have a much smaller aspect ratio than is usually observed for bassanite. It is possible that the cetrimonium bromide used in the experiments of Kong *et al.* is adsorbing to the surfaces of bassanite and preventing adsorption of Ca^{2+} or SO_4^{2-} ions, which may alter the morphology. The morphology of bassanite in Fig. 4(a) is also very similar to the morphology seen by Tang and Gao[67] when bassanite is grown in 0.008M disodium succinate, where the surface may also be protected from adsorbing ions.

The gypsum morphology bears a good resemblance to real-world crystals with a tabular crystal habit and the main {0 1 0} face adopting the shape of a parallelogram (see the work of Van Driessche, Stawski, and Kellermeier,[38] Fig. 2). Closer inspection, however, reveals that the main edge faces of the calculated morphology exhibit surfaces with the {0 2 1} and {1 1 0} Miller indices, whereas the edges of real gypsum crystals are predominantly the {0 2 1} and {−1 1 1} Miller indices[68] (note different indexing of gypsum used in the reference). Our calculated gypsum morphology does bear a strong resemblance to previous computationally predicted morphologies.[69–71] In particular, Aquilano *et al.*[71] proposed that the discrepancy may be due to the presence of stepped and kinked surface forms, which we have not thoroughly explored in our calculations.

We stress that these predicted morphologies are for large crystals in thermodynamic equilibrium. For small nanocrystals, edge and corner effects become more important and may alter the preferred morphology. Additionally, kinetic effects may also alter the growth mechanism and lead to different observed morphologies.

A couple of key quantities can be derived from the interfacial free energies and the predicted morphologies. First, we can express the surface area of the morphologies as a function of their volume. While it is possible to give a direct expression, it is more useful to describe the relationship as a deviation from a perfect sphere. The surface area of a sphere as a function of volume is given by

$$A_{Sphere} = 6^{2/3}\pi^{1/3}V^{2/3} = CV^{2/3}, \tag{24}$$

where A_{Sphere} is the surface area, V is the volume of the material, and C is the collection of constant terms. We can then derive a "shape factor" that describes the surface area of a morphology as a function of the surface area of a sphere of the same volume,

$$f_{Nano} = \frac{A_{Nano}}{A_{Sphere}}, \tag{25}$$

where f_{Nano} is the shape factor for the morphology. The shape factor is always greater than or equal to 1 as a sphere minimizes the surface area per unit volume of any 3D shape. Consequently the shape factor may be seen as a descriptor of "deviation from spherical" of a given morphology.

Another useful quantity is the average interfacial free energy of the morphology. This quantity is not simply the average of the computed interfacial free energies as the different surfaces contribute different amounts of surface area, depending on the lattice, Miller index, crystal symmetry, and interfacial free energy. Thus, the average interfacial free energy of the morphology is given by a weighted average over the expressed faces,

$$\gamma_{Nano} = \frac{\sum_{i=1}^{n_{faces}} \gamma_i A_i}{\sum_{i=1}^{n_{faces}} A_i}, \tag{26}$$

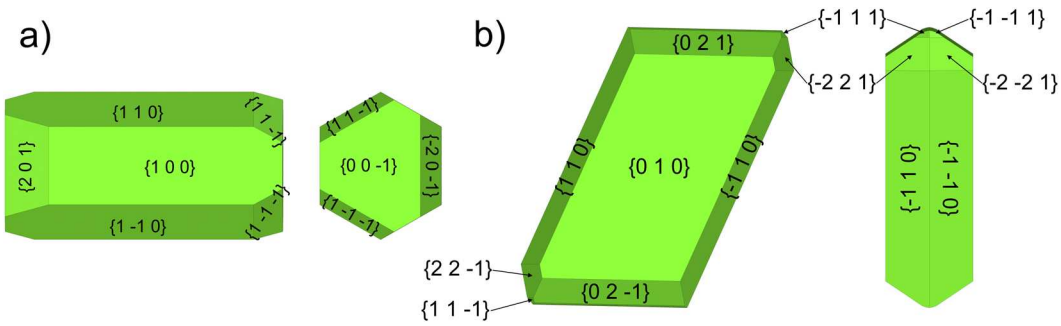

FIG. 4. Wulff construction of the equilibrium morphologies of (a) bassanite and (b) gypsum.

TABLE IV. Nanoparticle shape factors, nanoparticle interfacial free energies, and volume per formula unit of bassanite and gypsum.

	f_{Nano}	γ_{Nano} (J/m^2)	V_{Bulk} (Å^3)
Bassanite	1.22	0.0956	92.36
Gypsum	1.29	0.0751	128.20

where n_{faces} is the number of expressed faces on the nanoparticle and γ_i is the interfacial free energy of face i (note that a given Miller index may express more than one face due to symmetry). These quantities are readily available from the Wulff construction. Nanoparticle shape factors, nanoparticle interfacial free energies, and volume per formula unit for bassanite and gypsum are given in Table IV.

There is very little difference in the shape factors, but gypsum displays a slightly lower average interfacial free energy due to the dominant {0 1 0} surface. This small difference may go some way to explaining why bassanite is sometimes observed forming first in solution and sometimes not[38] as there may be very little difference in the free energy of the preferred phase for small nanoparticles.

To probe this further, we calculated the free energy to convert a bassanite nanoparticle into a gypsum nanoparticle in a solution of pure water. First, we derive a function that gives the free energy change of converting n formula units of bulk material into a nanoparticle of n formula units in contact with pure water,

$$\Delta F_{Bulk}^{Nano}(n) = \gamma_{Nano} f_{Nano} C (n V_{Bulk})^{2/3}. \tag{27}$$

Here, we have used Eq. (24) to calculate the surface area of a sphere composed of n formula units of bulk material. This surface area is then scaled by the shape factor, f_{Nano}, and multiplied by the average interfacial free energy of the morphology, γ_{Nano}.

The relative free energy between a bassanite and gypsum nanoparticle of the same number of $CaSO_4$ formula units is then given by the function

$$\Delta F_{Nano(Bas.)}^{Nano(Gyp.)}(n) = -\Delta F_{Bas.}^{Nano(Bas.)}(n) + n\Delta F_{Bas.}^{Gyp.} + \Delta F_{Gyp.}^{Nano(Gyp.)}(n). \tag{28}$$

The first term on the right-hand side of Eq. (28), $-\Delta F_{Bas.}^{Nano(Bas.)}(n)$, corresponds to converting a bassanite nanoparticle of n formula units of $CaSO_4$ into bulk bassanite. The second term, $n\Delta F_{Bas.}^{Gyp.}$, corresponds to converting n formula units of bulk bassanite into bulk gypsum using Eq. (22). The final term, $\Delta F_{Gyp.}^{Nano(Gyp.)}(n)$, corresponds to converting n formula units of bulk gypsum into a gypsum nanoparticle in contact with pure water.

Plotting the function given in Eq. (28) as a function of number of formula units (n) gives the graph in Fig. 5.

When the line in Fig. 5 is above the x axis, it indicates that a bassanite nanoparticle is more favorable to form than a gypsum nanoparticle. Conversely, below the x axis, it is more favorable for gypsum to form. Figure 5 clearly shows that a bassanite nanoparticle is unlikely to grow as the crossover point is at ~1 formula unit of $CaSO_4$, much too small for any "bassanite-like" features to be distinguishable.

However, it should be noted that the predicted crossover size of nanoparticle stability is highly sensitive to even small changes in the surface free energies. Increasing the average surface free energy of gypsum by just 5% is enough to change the crossover size from 1 formula unit to 22 formula units. In addition, the surface free energies of bassanite tend to have a greater entropic component than the surface free energies of gypsum. This greater entropic contribution suggests that the bassanite surface free energies will be more sensitive to temperature, as well as the presence of additional species in the liquid, which may disrupt the water ordering above the surface. These changes may easily be enough to swing the energy balance and make small nanoparticles of bassanite more stable than gypsum. Growth of bassanite nanoparticles from this point may then be controlled by kinetics, rather than thermodynamics.

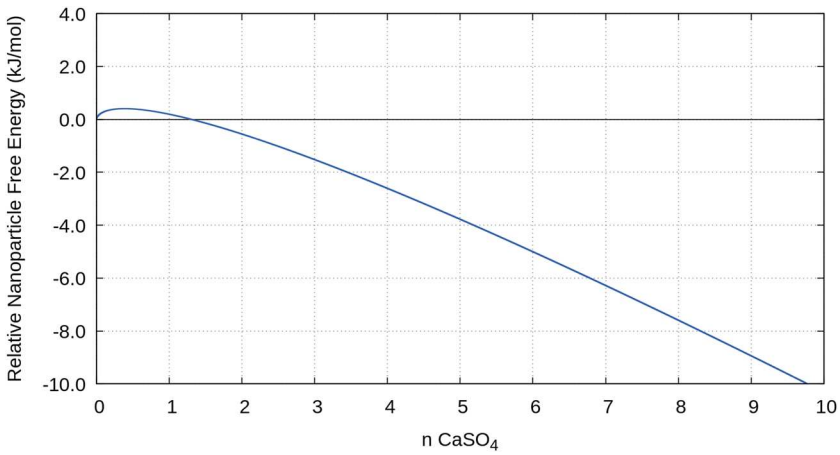

FIG. 5. Relative free energies of a gypsum nanoparticle compared to a bassanite nanoparticle as a function of $CaSO_4$ formula units.

V. CONCLUSIONS

We have demonstrated the development and application of a new, general, method for the calculation of interfacial free energies, which uses Einstein crystals as a common reference state. The new method is similar to the one proposed independently by Addula and Punnathanam[23] but in addition can handle surface diffusion of molecules belonging to the solid phase. Our method also includes further optimizations that increase the efficiency of calculating the interfacial free energy.

By using an Einstein crystal as a universal reference state, we are able to deal with complex materials and interfaces where other approaches would fail. When simulating liquid/solid/liquid systems, our approach does not require that the two surfaces of the solid slab are able to meet to re-form bulk and so can deal with complex surface motifs and reconstructions. The method is also able to handle interfaces with miscible species, which formally belong to the solid slab due to requirements to maintain constant composition but behave as a liquid at the interface. Furthermore, we have divided up the steps necessary to maximize the re-use of already computed values, saving significant computational resources [Sec. II B].

While we have primarily applied our method to the solid/liquid interface, there is no reason why our method cannot also be applied to transformation between polymorphs, solid/solid interfaces (such as grain boundaries), or many other types of defects. As long as the transformation to an Einstein crystal can be achieved continuously and reversibly, then the free energy of the defect can be computed. We have demonstrated the ability of the method to calculate the free energy of hydrating bassanite to gypsum, successfully reproducing the results of Byrne, Raiteri, and Gale,[44] which were computed via an alternative method (Sec. IV B).

We have applied our method to the interface of bassanite and gypsum with water and have demonstrated a significant entropic contribution to the interfacial free energies, frequently equal to or greater in size than the enthalpic contributions. Furthermore, the size of the entropic contributions varies significantly depending on the surface, and it is clear that a single universal entropy correction is not sufficient for predicting interfacial free energies (Sec. IV C).

In contrast to the $CaSO_4 \cdot xH_2O$ system, we demonstrated that the {1 0 0} surface of NaCl is dominated by the enthalpic contribution, with entropy playing a smaller role. We attribute this to the divalent nature of the ions in $CaSO_4 \cdot xH_2O$ as compared to the monovalent ions in NaCl and the subsequent increase in water ordering at the interface (Sec. IV D).

We have taken the calculated interfacial free energies of bassanite and gypsum and used them to predict equilibrium morphologies using a Wulff construction (Sec. IV E). The bassanite morphology bears a good resemblance to some experimental morphologies, retaining a hexagonal prism habit, but is somewhat shorter than the rod-like crystals often seen experimentally.[72,73] The predicted gypsum morphology differs from experimental morphologies in the proportion of the expressed edge faces but is in excellent agreement with other computationally predicted morphologies, indicating a common cause of the discrepancy.[71]

We used our calculated free energies along with the Wulff constructions to predict the thermodynamic crossover size of bassanite/gypsum nanoparticles (Sec. IV E). The results suggest that bassanite nanoparticles are almost always less stable than a gypsum nanoparticle of the same size. However, the crossover size is strongly dependent on even small changes to the surface free energies, and small changes to the conditions may make small bassanite nanoparticles more favorable than gypsum.

In future work, we will use our method to study other systems where the use of enthalpies alone is inadequate and understanding the interfacial free energies is vital. We will also work to extend our method to the calculation of interfaces with non-pure solutions, which will pose challenges in maintaining consistent solution concentrations. This extension to the method will be useful in studying the effect of additive species on different surfaces and how these may change the relative stability of bassanite and gypsum nanoparticles.

SUPPLEMENTARY MATERIAL

See supplementary material for bassanite and gypsum surface repeat units, 1D surface water density comparison between the NaCl {1 0 0} and bassanite {1 1 0}, 3D bassanite and gypsum morphologies and the LAMMPS input scripts used in this work.

ACKNOWLEDGMENTS

This work was supported by the "Crystallisation in the Real World" programme grant (EPSRC Grant No. EP/R018820/1). Calculations were performed using the Sulis Tier 2 HPC platform hosted by the Scientific Computing Research Technology Platform at the University of Warwick. Sulis is funded by EPSRC Grant No. EP/T022108/1 and the HPC Midlands+ consortium. Via our membership of the UK's HEC Materials Chemistry Consortium, which is funded by EPSRC (Grant No. EP/R029431), this work used the ARCHER2 UK National Supercomputing Service (http://www.archer2.ac.uk).

AUTHOR DECLARATIONS

Conflict of Interest

The authors have no conflicts to disclose.

Author Contributions

Stephen R. Yeandel: Conceptualization (equal); Data curation (lead); Formal analysis (lead); Investigation (lead); Methodology (lead); Visualization (lead); Writing – original draft (lead); Writing – review & editing (lead). **Colin L. Freeman**: Conceptualization (equal); Funding acquisition (equal); Project administration (equal). **John H. Harding**: Conceptualization (equal); Funding acquisition (equal); Project administration (equal).

DATA AVAILABILITY

Raw data were generated at the ARCHER2 and SULIS large scale HPC facilities. Derived data supporting the findings of this study are available from the corresponding author upon reasonable request.

APPENDIX A: THERMODYNAMIC INTEGRATION (TI)

To obtain the free energy difference between two different systems, we may integrate over an arbitrary thermodynamic pathway between the two systems of interest. We avoid changes to the atomic masses and so the kinetic energy contributions to the integral are zero, and we may focus on the potential energy contribution to the Hamiltonian, H. We use a control parameter, λ, to smoothly switch between the two systems,

$$H(\lambda) = (1-\lambda)H_A + \lambda H_B, \tag{A1}$$

where H_A is the Hamiltonian of system "A" and H_B is the Hamiltonian of system "B." When $\lambda = 0$, the system is in state "A," and when $\lambda = 1$, the system is in state "B." The change in free energy between the two systems is then given by the integral

$$\Delta F_A^B = \int_{\lambda=0}^{\lambda=1} \left\langle \frac{\partial H(\lambda)}{\partial \lambda} \right\rangle_\lambda d\lambda, \tag{A2}$$

where the angled brackets indicate an ensemble average for a given value of λ. The thermodynamic pathway is entirely arbitrary as long as it is both continuous and reversible. Using λ directly may cause numerical convergence issues when λ approaches 0 or 1. To avoid these issues, we use a function of λ instead,

$$f(\lambda) = \lambda^5\left(70\lambda^4 - 315\lambda^3 + 540\lambda^2 - 420\lambda + 126\right), \tag{A3}$$

which is a sigmoid function of λ with useful properties that improve convergence.[74,75] The switching function given in Eq. (A3) smoothly approaches zero as λ approaches 0 or 1, improving convergence of the integral. To obtain $\partial H(\lambda)/\partial\lambda$ as required in Eq. (A2), we then use the chain rule,

$$\frac{\partial H(\lambda)}{\partial \lambda} = \frac{\partial H(f(\lambda))}{\partial f(\lambda)} \frac{\partial f(\lambda)}{\partial \lambda}, \tag{A4}$$

where $\partial f(\lambda)/\partial\lambda$ is given analytically by

$$\frac{\partial f(\lambda)}{\partial \lambda} = 630\left(\lambda^2 - \lambda\right)^4. \tag{A5}$$

This substitution of $f(\lambda)$ for λ is equivalent to a re-weighting scheme for the integral given in Eq. (A2). The use of Eq. (A3) results in reduced sampling near $\lambda = 0.5$ and increased sampling as λ approaches 0 or 1. Equation (A5) then gives weights for the new integral points. To obtain the value of $\partial H(f(\lambda))/\partial f(\lambda)$, we use numerical differentiation of the potential energy by a symmetric difference quotient,

$$\frac{\partial H(f(\lambda))}{\partial f(\lambda)} \approx \frac{H(f(\lambda)+\delta) - H(f(\lambda)-\delta)}{2\delta}. \tag{A6}$$

As $f(\lambda)$ varies non linearly with respect to λ a fixed value of δ for all values of λ may lead to numerical issues when $f(\lambda)$ becomes very small. i.e., if $f(\lambda)$ is very small and δ is relatively large, then the perturbed potential may have a negative coefficient. To alleviate this, we also make δ a function of λ,

$$\delta(\lambda) = 0.01 \times f(\lambda). \tag{A7}$$

To compute the value of $\partial H(f(\lambda))/\partial f(\lambda)$, we first run a simulation for a given value of λ, printing the simulation trajectory frequently. The potential energy at each frame of the trajectory is averaged together to obtain $H(f(\lambda))$. The values of $H(f(\lambda)+\delta(\lambda))$ and $H(f(\lambda)-\delta(\lambda))$ are calculated by taking the trajectory used to calculate $H(f(\lambda))$ and recalculating the average potential energy with $f(\lambda) \pm \delta(\lambda)$. This is possible because for a very small perturbation of $f(\lambda)$, the accessible phase space will be almost identical and a second (or third) new simulation is not required to sample it, saving significant simulation time. Another advantage with this approach is that δ may be tuned *a posteriori* if the derivative obtained from Eq. (A6) is poorly behaved due to the choice of δ.

The integral in Eq. (A2) is computed numerically via Romberg's method (The trapezoidal rule with Richardson extrapolation). Romberg's method requires successively dividing the integration interval into two equal halves. The change in the estimate of the integral (via the trapezoidal rule) over the increasing subdivisions is used to extrapolate an improved estimate for the integral, canceling leading order terms due to the curvature of the integrand. Furthermore, as the number of points in the integrand is doubled for each Romberg iteration, we can estimate the error of the free energy based on the convergence from one iteration to the next.

APPENDIX B: THE DIFFERENCE BETWEEN SURFACE TENSION AND INTERFACIAL FREE ENERGY

The method of Kirkwood and Buff[26] (Sec. II C) is able to calculate the surface tension of a liquid. However, it is inapplicable to interfaces with a solid component (such as solid/vacuum, solid/fluid, or solid/solid) as the surface tension differs from the interfacial free energy. The relationship between surface tension and interfacial free energy as given by Shuttleworth[76] is

$$\sigma = \gamma + A\left(\frac{d\gamma}{dA}\right), \tag{B1}$$

where σ is the surface tension, γ is the interfacial free energy, and A is the surface area. The second term on the right-hand side is zero for liquids, as expanding the surface area simply creates more surface, leaving the interfacial free energy unchanged. For solids, however, expanding the surface results in a strained surface (altering γ), and the second term is non-zero. This point has been expanded upon and discussed by others previously.[5,77]

APPENDIX C: CORRECTION FOR MISCIBLE SPECIES IN NON-PURE SOLUTIONS

The procedure outlined in Sec. II F is applicable for liquids that comprise a single species. This is because transforming the entirety

of the bulk liquid simulation cell to an Einstein crystal and dividing by the number of transformed molecules is equivalent to transforming a single molecule to an Einstein crystal and leaving the rest of the simulation cell in the liquid state (with an adjustment to the correct density).

When the liquid is a solution that contains multiple different molecular species, this approach is not possible as it would result in a free energy that is an average over the different species. To obtain a free energy for a particular molecular species, two solutions should be created; the first at the desired concentration and the second at the desired concentration plus one additional molecule of the species of interest. Transforming both to Einstein crystals and taking the difference yields the free energy of transforming the single molecular species to an Einstein crystal from the solution, under the approximation of no change in solution concentration. An extrapolation to infinitely small changes in concentration by using multiple simulation cell sizes may also be useful.

It must be emphasized that the correction outlined in Sec. II F is only applicable when the solid/liquid system is near equilibrium. If the solid is highly soluble, then we are not dealing with miscible species, but dissolution of the solid. Eventually, the system may reach an equilibrium with a concentrated solution. If there is still a well-defined interface between the solid and liquid, then the methods in this paper will still be applicable, but the liquid phase will now be a concentrated solution, and all values (such as the surface tension, Sec. II C) should be calculated with respect to the concentrated solution. If a correction for restoring stoichiometry due to miscible surface species is still required, it can be performed as before.

REFERENCES

[1] S. Kerisit and S. C. Parker, "Free energy of adsorption of water and metal ions on the {1014} calcite surface," J. Am. Chem. Soc. **126**, 10152–10161 (2004).

[2] J. Q. Broughton and G. H. Gilmer, "Molecular dynamics investigation of the crystal–fluid interface. VI. Excess surface free energies of crystal–liquid systems," J. Chem. Phys. **84**, 5759–5768 (1986).

[3] R. Benjamin and J. Horbach, "Crystal-liquid interfacial free energy via thermodynamic integration," J. Chem. Phys. **141**, 044715 (2014).

[4] R. Benjamin and J. Horbach, "Crystal-liquid interfacial free energy of hard spheres via a thermodynamic integration scheme," Phys. Rev. E **91**, 032410 (2015).

[5] X. Qi, Y. Zhou, and K. A. Fichthorn, "Obtaining the solid-liquid interfacial free energy via multi-scheme thermodynamic integration: Ag-ethylene glycol interfaces," J. Chem. Phys. **145**, 194108 (2016).

[6] V. Ballenegger, "Communication: On the origin of the surface term in the Ewald formula," J. Chem. Phys. **140**, 161102 (2014).

[7] V. Ballenegger, A. Arnold, and J. J. Cerdà, "Simulations of non-neutral slab systems with long-range electrostatic interactions in two-dimensional periodic boundary conditions," J. Chem. Phys. **131**, 094107 (2009).

[8] A. Malani, A. Raghavanpillai, E. B. Wysong, and G. C. Rutledge, "Can dynamic contact angle be measured using molecular modeling?," Phys. Rev. Lett. **109**, 184501 (2012).

[9] S. Angioletti-Uberti, M. Ceriotti, P. D. Lee, and M. W. Finnis, "Solid-liquid interface free energy through metadynamics simulations," Phys. Rev. B **81**, 125416 (2010).

[10] S. Angioletti-Uberti, "The solid–liquid interface free-energy of Pb: Comparison of theory and experiments," J. Phys.: Condens. Matter **23**, 435008 (2011).

[11] J. R. Espinosa, C. Vega, and E. Sanz, "The mold integration method for the calculation of the crystal-fluid interfacial free energy from simulations," J. Chem. Phys. **141**, 134709 (2014).

[12] J. R. Espinosa, C. Vega, C. Valeriani, and E. Sanz, "The crystal-fluid interfacial free energy and nucleation rate of NaCl from different simulation methods," J. Chem. Phys. **142**, 194709 (2015).

[13] J. R. Espinosa, C. Vega, and E. Sanz, "Ice–water interfacial free energy for the TIP4P, TIP4P/2005, TIP4P/ice, and mW models as obtained from the mold integration technique," J. Phys. Chem. C **120**, 8068–8075 (2016).

[14] B. Cheng, G. A. Tribello, and M. Ceriotti, "Solid-liquid interfacial free energy out of equilibrium," Phys. Rev. B **92**, 180102 (2015).

[15] F. Schmitz and P. Virnau, "The ensemble switch method for computing interfacial tensions," J. Chem. Phys. **142**, 144108 (2015).

[16] A. R. Nair and S. P. Sathian, "A molecular dynamics study to determine the solid-liquid interfacial tension using test area simulation method (TASM)," J. Chem. Phys. **137**, 084702 (2012).

[17] E. M. Grzelak and J. R. Errington, "Computation of interfacial properties via grand canonical transition matrix Monte Carlo simulation," J. Chem. Phys. **128**, 014710 (2008).

[18] F. Leroy and F. Müller-Plathe, "Solid-liquid surface free energy of Lennard-Jones liquid on smooth and rough surfaces computed by molecular dynamics using the phantom-wall method," J. Chem. Phys. **133**, 044110 (2010).

[19] X.-M. Bai and M. Li, "Calculation of solid-liquid interfacial free energy: A classical nucleation theory based approach," J. Chem. Phys. **124**, 124707 (2006).

[20] R. L. Davidchack and B. B. Laird, "Direct calculation of the crystal–melt interfacial free energies for continuous potentials: Application to the Lennard-Jones system," J. Chem. Phys. **118**, 7651–7657 (2003).

[21] J. J. Hoyt, M. Asta, and A. Karma, "Method for computing the anisotropy of the solid-liquid interfacial free energy," Phys. Rev. Lett. **86**, 5530 (2001).

[22] A. Einstein, "Die plancksche theorie der strahlung und die theorie der spezifischen wärme," Ann. Phys. **327**, 180–190 (1907).

[23] R. K. R. Addula and S. N. Punnathanam, "Computation of solid–fluid interfacial free energy in molecular systems using thermodynamic integration," J. Chem. Phys. **153**, 154504 (2020).

[24] D. Frenkel and A. J. C. Ladd, "New Monte Carlo method to compute the free energy of arbitrary solids. Application to the FCC and HCP phases of hard spheres," J. Chem. Phys. **81**, 3188–3193 (1984).

[25] D. Frenkel and B. Smit, *Understanding Molecular Simulation: From Algorithms to Applications*, 2nd ed. (Elsevier, 2002).

[26] J. G. Kirkwood and F. P. Buff, "The statistical mechanical theory of surface tension," J. Chem. Phys. **17**, 338–343 (1949).

[27] K. Fuchs, "A quantum mechanical investigation of the cohesive forces of metallic copper," Proc. R. Soc. London, Ser. A **151**, 585–602 (1935).

[28] M. A. Kastenholz and P. H. Hünenberger, "Computation of methodology-independent ionic solvation free energies from molecular simulations. I. The electrostatic potential in molecular liquids," J. Chem. Phys. **124**, 124106 (2006).

[29] M. A. Kastenholz and P. H. Hünenberger, "Computation of methodology-independent ionic solvation free energies from molecular simulations. II. The hydration free energy of the sodium cation," J. Chem. Phys. **124**, 224501 (2006).

[30] T. Darden, D. Pearlman, and L. G. Pedersen, "Ionic charging free energies: Spherical versus periodic boundary conditions," J. Chem. Phys. **109**, 10921–10935 (1998).

[31] T. L. Hill, *An Introduction to Statistical Thermodynamics* (Courier Corporation, 1986).

[32] V. Khanna, J. Anwar, D. Frenkel, M. F. Doherty, and B. Peters, "Free energies of crystals computed using Einstein crystal with fixed center of mass and differing spring constants," J. Chem. Phys. **154**, 164509 (2021).

[33] W. G. Hoover and F. H. Ree, "Melting transition and communal entropy for hard spheres," J. Chem. Phys. **49**, 3609–3617 (1968).

[34] J. E. Jones, "On the determination of molecular fields.—I. From the variation of the viscosity of a gas with temperature," Proc. R. Soc. London, Ser. A **106**, 441–462 (1924).

[35]J. E. Jones, "On the determination of molecular fields.—II. From the equation of state of a gas," Proc. R. Soc. London, Ser. A **106**, 463–477 (1924).
[36]T. C. Beutler, A. E. Mark, R. C. van Schaik, P. R. Gerber, and W. F. Van Gunsteren, "Avoiding singularities and numerical instabilities in free energy calculations based on molecular simulations," Chem. Phys. Lett. **222**, 529–539 (1994).
[37]P. Ballirano, A. Maras, S. Meloni, and R. Caminiti, "The monoclinic I2 structure of bassanite, calcium sulphate hemihydrate ($CaSO_4 \cdot 0.5H_2O$)," Eur. J. Mineral. **13**, 985–993 (2001).
[38]A. E. S. Van Driessche, T. M. Stawski, and M. Kellermeier, "Calcium sulfate precipitation pathways in natural and engineered environments," Chem. Geol. **530**, 119274 (2019).
[39]P. Comodi, S. Nazzareni, P. F. Zanazzi, and S. Speziale, "High-pressure behavior of gypsum: A single-crystal X-ray study," Am. Mineral. **93**, 1530–1537 (2008).
[40]A. E. S. Van Driessche, L. G. Benning, J. D. Rodriguez-Blanco, M. Ossorio, P. Bots, and J. M. García-Ruiz, "The role and implications of bassanite as a stable precursor phase to gypsum precipitation," Science **336**, 69–72 (2012).
[41]F. C. Hawthorne and R. B. Ferguson, "Anhydrous sulphates. II. Refinement of the crystal structure of anhydrite," Can. Mineral. **13**, 289–292 (1975), available at https://pubs.geoscienceworld.org/canmin/issue/13/3.
[42]G. A. Lager, T. Armbruster, F. J. Rotella, J. D. Jorgensen, and D. G. Hinks, "A crystallographic study of the low-temperature dehydration products of gypsum, $CaSO_4 \cdot 2H_2O$: Hemihydrate, $CaSO_4 \cdot 0.50H_2O$, and $\gamma - CaSO_4$," Am. Mineral. **69**, 910–919 (1984), available at http://www.minsocam.org/msa/collectors_corner/amtoc/toc1984.htm.
[43]B. S. Krumgalz, "Temperature dependence of mineral solubility in water. Part 3. Alkaline and alkaline earth sulfates," J. Phys. Chem. Ref. Data **47**, 023101 (2018).
[44]E. H. Byrne, P. Raiteri, and J. D. Gale, "Computational insight into calcium–sulfate ion pair formation," J. Phys. Chem. C **121**, 25956–25966 (2017).
[45]J. Bokeloh, G. Wilde, R. E. Rozas, R. Benjamin, and J. Horbach, "Nucleation barriers for the liquid-to-crystal transition in simple metals: Experiment vs. simulation," Eur. Phys. J.: Spec. Top. **223**, 511–526 (2014).
[46]G. W. Watson, E. T. Kelsey, N. H. de Leeuw, D. J. Harris, and S. C. Parker, "Atomistic simulation of dislocations, surfaces and interfaces in MgO," J. Chem. Soc., Faraday Trans. **92**, 433–438 (1996).
[47]S. Plimpton, "Fast parallel algorithms for short-range molecular dynamics," J. Comput. Phys. **117**, 1–19 (1995).
[48]R. W. Hockney and J. W. Eastwood, *Computer Simulation Using Particles* (CRC Press, 1988).
[49]S. Nosé, "A unified formulation of the constant temperature molecular dynamics methods," J. Chem. Phys. **81**, 511–519 (1984).
[50]W. G. Hoover, "Canonical dynamics: Equilibrium phase-space distributions," Phys. Rev. A **31**, 1695 (1985).
[51]T. Schneider and E. Stoll, "Molecular-dynamics study of a three-dimensional one-component model for distortive phase transitions," Phys. Rev. B **17**, 1302 (1978).
[52]F. Legoll, M. Luskin, and R. Moeckel, "Non-ergodicity of the Nosé–Hoover thermostatted harmonic oscillator," Arch. Ration. Mech. Anal. **184**, 449–463 (2007).
[53]Y. Wu, H. L. Tepper, and G. A. Voth, "Flexible simple point-charge water model with improved liquid-state properties," J. Chem. Phys. **124**, 024503 (2006).
[54]T. M. Stawski, A. E. S. Van Driessche, R. Besselink, E. H. Byrne, P. Raiteri, J. D. Gale, and L. G. Benning, "The structure of $CaSO_4$ nanorods: The precursor of gypsum," J. Phys. Chem. C **123**, 23151–23158 (2019).
[55]M. P. Allen and D. J. Tildesley, *Computer Simulation of Liquids* (Oxford University Press, 2017).
[56]H. Sun, "COMPASS: An ab initio force-field optimized for condensed-phase applications overview with details on alkane and benzene compounds," J. Phys. Chem. B **102**, 7338–7364 (1998).
[57]J. Mei, J. W. Davenport, and G. W. Fernando, "Analytic embedded-atom potentials for FCC metals: Application to liquid and solid copper," Phys. Rev. B **43**, 4653 (1991).
[58]T. A. Pascal and W. A. Goddard III, "Interfacial thermodynamics of water and six other liquid solvents," J. Phys. Chem. B **118**, 5943–5956 (2014).
[59]S. P. Kadaoluwa Pathirannahalage, N. Meftahi, A. Elbourne, A. C. G. Weiss, C. F. McConville, A. Padua, D. A. Winkler, M. Costa Gomes, T. L. Greaves, T. C. Le *et al.*, "Systematic comparison of the structural and dynamic properties of commonly used water models for molecular dynamics simulations," J. Chem. Inf. Model. **61**, 4521–4536 (2021).
[60]N. R. Pallas and Y. Harrison, "An automated drop shape apparatus and the surface tension of pure water," Colloids Surf. **43**, 169–194 (1990).
[61]D. D. Wagman, W. H. Evans, V. B. Parker, R. H. Schumm, I. Halow, S. M. Bailey, K. L. Churney, and R. L. Nuttal, "Selected values for inorganic and C1 and C2 organic substances in SI units," J. Phys. Chem. Ref. Data **11**, Suppl. No. 2 (1982), available at https://www.nist.gov/srd/journal-physical-and-chemical-reference-data-monographs-or-supplements.
[62]R. K. Mishra, K. Kanhaiya, J. J. Winetrout, R. J. Flatt, and H. Heinz, "Force field for calcium sulfate minerals to predict structural, hydration, and interfacial properties," Cem. Concr. Res. **139**, 106262 (2021).
[63]I. S. Joung and T. E. Cheatham III, "Determination of alkali and halide monovalent ion parameters for use in explicitly solvated biomolecular simulations," J. Phys. Chem. B **112**, 9020–9041 (2008).
[64]M. Bruno, D. Aquilano, L. Pastero, and M. Prencipe, "Structures and surface energies of (100) and octopolar (111) faces of halite (NaCl): An ab initio quantum-mechanical and thermodynamical study," Cryst. Growth Des. **8**, 2163–2170 (2008).
[65]G. Wulff, "XXV. Zur frage der geschwindigkeit des wachsthums und der auflösung der krystallflächen," Z. Kristallogr. - Cryst. Mater. **34**, 449–530 (1901).
[66]B. Kong, B. Guan, M. Z. Yates, and Z. Wu, "Control of α-calcium sulfate hemihydrate morphology using reverse microemulsions," Langmuir **28**, 14137–14142 (2012).
[67]Y. Tang and J. Gao, "Investigation of the effects of sodium dicarboxylates on the crystal habit of calcium sulfate α-hemihydrate," Langmuir **33**, 9637–9644 (2017).
[68]A. J. Pinto, E. Ruiz-Agudo, C. V. Putnis, A. Putnis, A. Jiménez, and M. Prieto, "AFM study of the epitaxial growth of brushite ($CaHPO_4 \cdot 2H_2O$) on gypsum cleavage surfaces," Am. Mineral. **95**, 1747–1757 (2010).
[69]F. R. Massaro, M. Rubbo, and D. Aquilano, "Theoretical equilibrium morphology of gypsum ($CaSO_4 \cdot 2H_2O$). 1. A syncretic strategy to calculate the morphology of crystals," Cryst. Growth Des. **10**, 2870–2878 (2010).
[70]F. R. Massaro, M. Rubbo, and D. Aquilano, "Theoretical equilibrium morphology of gypsum ($CaSO_4 \cdot 2H_2O$). 2. The stepped faces of the main [001] zone," Cryst. Growth Des. **11**, 1607–1614 (2011).
[71]D. Aquilano, F. Otálora, L. Pastero, and J. M. García-Ruiz, "Three study cases of growth morphology in minerals: Halite, calcite and gypsum," Prog. Cryst. Growth Charact. Mater. **62**, 227–251 (2016).
[72]U. Tritschler, M. Kellermeier, C. Debus, A. Kempter, and H. Cölfen, "A simple strategy for the synthesis of well-defined bassanite nanorods," CrystEngComm **17**, 3772–3776 (2015).
[73]Q. Chen, C. Jia, Y. Li, J. Xu, B. Guan, and M. Z. Yates, "α-calcium sulfate hemihydrate nanorods synthesis: A method for nanoparticle preparation by mesocrystallization," Langmuir **33**, 2362–2369 (2017).
[74]M. de Koning and A. Antonelli, "Einstein crystal as a reference system in free energy estimation using adiabatic switching," Phys. Rev. E **53**, 465 (1996).
[75]V. Fantauzzo, S. R. Yeandel, C. L. Freeman, and J. H. Harding, "A transferable force-field for alkali metal nitrates," J. Phys. Commun. **6**, 055011 (2022).
[76]R. Shuttleworth, "The surface tension of solids," Proc. Phys. Soc., London, Sect. A **63**, 444 (1950).
[77]R. Dingreville and J. Qu, "Interfacial excess energy, excess stress and excess strain in elastic solids: Planar interfaces," J. Mech. Phys. Solids **56**, 1944–1954 (2008).